Ultramicroscopy 110 (2010) 1143–1147

Contents lists available at ScienceDirect

Ultramicroscopy

journal homepage: www.elsevier.com/locate/ultramic

# Scanning transmission X-ray microscopy with a fast framing pixel detector

A. Menzel [a,*], C.M. Kewish [b,1], P. Kraft [a], B. Henrich [a], K. Jefimovs [c], J. Vila-Comamala [a], C. David [a], M. Dierolf [d,2], P. Thibault [d,1], F. Pfeiffer [d,2], O. Bunk [a]

[a] Paul Scherrer Institut, 5232 Villigen PSI, Switzerland
[b] Synchrotron SOLEIL, L'Orme des Merisiers, BP 48, Saint Aubin, 91192 Gif sur Yvette, France
[c] EMPA, 8600 Dübendorf, Switzerland
[d] Department Physik (E17), Technische Universität München, 85748 Garching, Germany

ARTICLE INFO

*Article history:*
Received 5 January 2009
Received in revised form
14 April 2010
Accepted 15 April 2010

*Keywords:*
Scanning transmission X-ray microscopy
Phase contrast
X-ray microscopy

ABSTRACT

Scanning transmission X-ray microscopy (STXM) is a powerful imaging technique, in which a small X-ray probe is raster scanned across a specimen. Complete knowledge of the complex-valued transmission function of the specimen can be gained using detection schemes whose every-day use, however, is often hindered by the need of specialized configured detectors or by slow or noisy readout of area detectors. We report on sub-50 nm-resolution STXM studies in the hard X-ray regime using the PILATUS, a fully pixelated fast framing detector operated in single-photon counting mode. We demonstrate a range of imaging modes, including phase contrast and dark-field imaging.



## 1. Introduction

X-ray imaging, in particular X-ray microscopy, offers several unique advantages for the characterization of life and materials science samples on the micron and sub-micron length scales. The penetration power of hard X-rays enables high-resolution studies of specimens several hundred microns thick, and the chemical specificity of X-rays allows, for instance, mapping the distribution of spurious metal compounds in organic or inorganic micro-structures.

In its basic form scanning transmission X-ray microscopy (STXM) records the photon flux past the specimen and assigns a transmission value to each position of illumination. Fast detector readout is crucial because scans frequently include tens of thousands of points. Single-element detectors add essentially no delay to the scanning process. However, it was recognized early on that more advanced detection schemes offer qualitatively different and complementary sample information, such as phase contrast or dark-field images [1–9]. For instance, a phase gradient that does not vary significantly over the area of illumination can be determined by measuring the shift of the illumination in the detector plane.

To facilitate imaging in these complementary modes, hardware solutions such as apertured or segmented detectors have been used [1–6]. These are usually optimized for a specific experimental geometry, and subsequent changes of the optical layout tend to have a detrimental effect on image quality [10]. In contrast, fully pixelated detectors promise unprecedented flexibility. However, their slow and relatively noisy readout has, so far, drastically limited their every-day use in scanning microscopes [7–9].

## 2. Experimental

We report on STXM measurements with a state-of-the-art area detector at the coherent small-angle X-ray scattering beamline (cSAXS) at the Swiss Light Source, Paul Scherrer Institut (PSI), Villigen, Switzerland. The PILATUS detector is a modular pixel detector [11], where each pixel of size $172 \times 172\,\mu m^2$ is individually equipped with a 20 bit single-photon counter. This design not only offers unprecedented dynamic range, but eliminates readout noise and has a point spread function extending over only one pixel.

The experimental setup is shown in Fig. 1. For measurements presented here, we used two different focusing optics. As high-efficiency Fresnel zone plate we used a 1 μm thick gold FZP with 75 μm diameter and 100 nm finest zone width [12] for producing the X-ray probe. With a source size of $200 \times 20\,\mu m^2$ (horizontal × vertical), a distance of ~34 m from the source, and a wavelength of 2 Å we expect a focal spot size, which is zone plate limited in the vertical plane, whereas horizontally the spot size is

* Corresponding author.
*E-mail address:* andreas.menzel@psi.ch (A. Menzel).
[1] Until recently: Paul Scherrer Institut.
[2] Until recently: Paul Scherrer Institut and École Polytechnique Fédérale de Lausanne, 1015 Lausanne, Switzerland.

0304-3991/$ - see front matter © 2010 Elsevier B.V. All rights reserved.
doi:10.1016/j.ultramic.2010.04.007

source size limited. The resultant probe has the dimensions of $\sim 300 \times 100$ nm (horizontal $\times$ vertical). For higher-resolution images, we use an FZP with a diameter of 50 μm and an outermost zone of 20 nm made of 350 nm thick iridium. These devices were fabricated with a zone doubling technique that bypasses the electron beam lithography limitations [13]. The increased numerical aperture results in the probe being significantly smaller than 50 nm in both dimensions. Originally these zone plates have been optimized for soft X-rays and are rather inefficient even at the lowest photon energy the cSAXS facility can provide, thereby increasing the acquisition time when sub-50 nm resolution is aimed at. The manufacturing of such zone plates, more appropriate for hard X-rays, is in progress.

An 11 μm pinhole was used as order-sorting aperture, i.e., to discriminate higher diffraction orders from the focusing zone plate. A central beam stop was placed upstream of the zone plate in order to block undiffracted light. Central stops of various diameters were prepared on a $\sim 20$ μm thick silicon membrane, on which a thin metal contact layer (20 nm Cr+20 nm Au) and a 200 nm thick PMMA resist layer were deposited. After electron beam exposure and development of the resist layer gold was plated into the resist opening to a thickness of 12 μm. Since the plated thickness is much higher than the resist thickness, the isotropic growth leads to an increase of the central stop diameter and to rounded edges, as shown in the inset of Fig. 1.

The photon energy selected for these measurements was 6.2 keV, at which the detective quantum efficiency of the PILATUS detector is essentially unity. We either employed a single PILATUS module, which comprises 100 kilopixels, or a two-module readout mode of the 24-module "PILATUS 2M". In each case, we analyzed a region of interest of $128 \times 128$ pixels centered around the unrefracted beam. The typical acquisition time per image point was chosen on the order of 10 ms, or up to 100 ms in case of highly focusing zone-doubled FZP prototypes [13]. Faster readout of the detector is possible. A single module can be read out within 3 ms and in the two-module readout mode the data transfer from the 2M detector takes $\sim 8$ ms. Increasing the acquisition rate thus introduces undue gaps in on-the-fly scans. Scanning pointwise, on the other hand, is currently rate limited by piezo settling time and feedback communication.

Fig. 2 shows X-ray micrographs of a zone-doubled grating with 50 nm spaced iridium lines, which was used as a test object to assess the contrast and resolution of the instrument. Transmission has been determined by integrating photon counts, $I$, over a detector area that completely included the illuminating annulus and was normalized by the maximum detected flux, $I_0$. The resolution should correspond to the size of the focal spot, which is verified by line scans. Insets show such line scans. The 25 nm lines and spaces are clearly resolved in the transmission measurement.

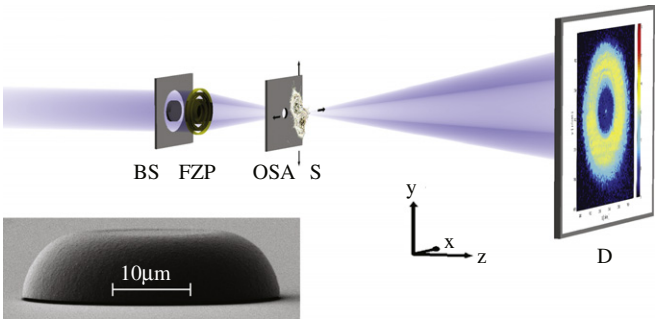


**Fig. 1.** Schematic of the experimental setup. Elements from left to right: beam-defining aperture combined with a central beam stop (BS); Fresnel zone plate (FZP); order-sorting aperture (OSA); specimen (S); detector (D). Inset: electron micrograph of a Au beamstop with 34 μm diameter and 8.5 μm thickness.

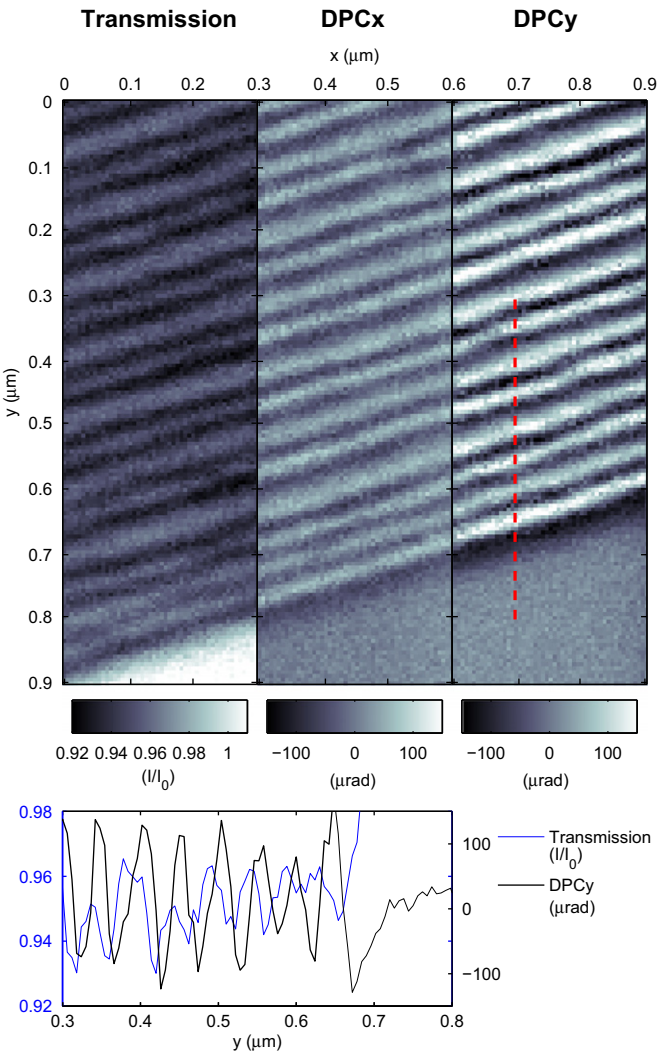


**Fig. 2.** Transmission, horizontal DPC, and vertical DPC images of a zone-doubled grating made of Ir. Field of view is $10 \times 30$ μm$^2$. Additionally we show a line scan through some of the finest structures of the test object, clearly resolving 25 nm lines and spaces, both in transmission (blue solid line) and differential phase contrast (black dashed line). The location of the line scan is marked by a red line in the STXM images. (For interpretation of the references to colour in this figure legend, the reader is referred to the web version of this article.)

Also contained in Fig. 2 are differential phase contrast (DPC) images, showing both horizontal and vertical phase gradients. Since its inception [14] in visible-light microscopy, DPC has been very popular in a wide field of imaging applications. However, beyond mere contrast enhancement one is often interested in knowledge of the specimen's complex-valued transmission function. Such complete knowledge allows essentially arbitrary imaging modes, an option that has been called "omni-microscopy" by some authors [15]. Thus, transmission measurements need to be combined with information of the absolute phase shift, which can be gained by integrating DPC signals. A reliable and highly robust integration method has been used, *inter alia*, in [16–18].

While ultimately deriving an equivalent expression, we choose a minimization approach, which allows one to judge in what respect the resulting phase estimate is optimal. We define as cost function

$$\chi^2 \equiv \sum_{i,j} \left( \left( \phi^x_{i,j} - \frac{\Delta \hat{\phi}_{i,j}}{\Delta x} \right)^2 + \left( \phi^y_{i,j} - \frac{\Delta \hat{\phi}_{i,j}}{\Delta y} \right)^2 \right), \quad (1)$$

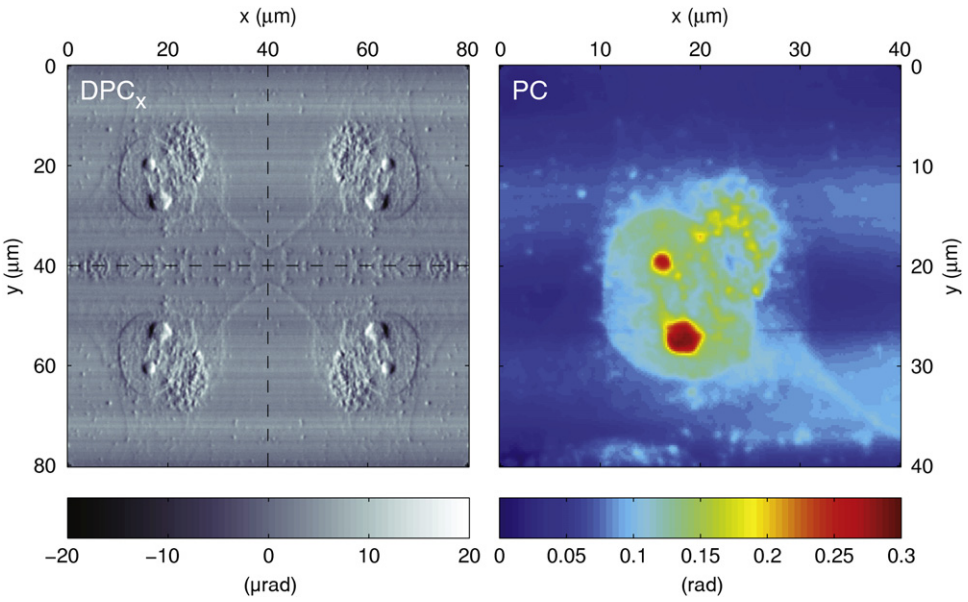


**Fig. 3.** Differential phase contrast image (left) and integrated phase (right) of the cytoskeleton of a human pancreatic cell. Measured DPC data are in the upper left quadrant of the DPC image. The rest of the DPC image is due to padding and symmetrization, the "seams" of which are emphasized by dashed lines.

where $\phi^x$ and $\phi^y$ denote the measured DPC signals in $x$ and $y$, and $\hat{\phi}$ marks the estimate of the integrated phase. The search for a minimum, i.e., $\partial\chi^2/\partial\hat{\phi}=0$, yields the Poisson equation, $\partial\phi^x/\partial x+\partial\phi^y/\partial y=\nabla^2\hat{\phi}$. Various efficient methods exist to solve this equation numerically [19]. After padding and symmetrization, as sketched in Fig. 3, a fast solution based on Fourier transforms can be used:

$$\hat{\phi}=\mathrm{i}\mathcal{F}^{-1}\left\{\frac{q_x\tilde{\phi}^x+q_y\tilde{\phi}^y}{q_x^2+q_y^2}\right\}, \tag{2}$$

where $\tilde{\phi}^{x,y}$ marks the Fourier transforms of the DPC signal $\phi^{x,y}$, $q_{x,y}$ denotes the momentum transfer, and $\mathcal{F}^{-1}$ is the inverse Fourier transform operator. We note that Eq. (2) is equivalent to the real part of, e.g., Eq. (4) of [17], whose imaginary part can be interpreted as signifying mismatch between measured $\phi^x$ and $\phi^y$.

This integration can be performed virtually instantaneously, and we find it advantageous to integrate both DPC signals and display the integral's derivatives. Taking this into account the coupling between $\phi^x$ and $\phi^y$ often reduces noise. All DPC images in Figs. 2–4 were produced this way.

The line scans in Fig. 2 reveal the excellent signal-to-noise ratio of DPC measurements. Poisson statistics dictates that the error in absorption measurements scales with $\sqrt{I}/I_0$, whereas the error measuring the angle of refraction scales with $\mathcal{N}_A/\sqrt{I}$ [20], with $\mathcal{N}_A$ being the numerical aperture of the focusing optics, in our case $\sim 1/1000$. Consequently, the statistical uncertainty, for instance, estimating the thickness of material based on DPC is reduced by $\sim\mathcal{N}_A$ compared to the uncertainty resultant of absorption measurements.

We further note that the DPC measurement is inherently insensitive to many systematic errors, such as beam intensity fluctuations. In Fig. 3 we show a specimen with significantly weaker contrast. The cytoskeleton of a Panc1 human pancreatic cell was extracted, fixated with glutaldehye and osmium tetroxide, and dehydrated. Analog to the preparation for transmission electron micrographs, uranyl acetate was used to enhance contrast. Nevertheless, the maximum angle of X-ray refraction is $\sim 20\,\mu$rad, i.e., about a quarter of a PILATUS pixel at the detector distance of 2.2 m. The statistical noise in the DPC signal for this measurement is $\sim 200$ nrad, as estimated from measured fluctuations from the empty membrane. For the phase integration, shown in Fig. 3, the DPC signals were background subtracted, which is equivalent to defining the $\vec{q}=0$ position on the detector. The measured signal was symmetrically padded in order to prevent periodicity artefacts and to ensure Neumann boundary conditions. This analysis can be performed "on the fly", i.e., the microscopist obtains immediate feedback and results.

Dark-field imaging, as a further measurement modality of the instrument, is demonstrated in Fig. 4. Comparing the detected flux inside and outside of the illumination annulus shown in Fig. 1 allows quantitative measurements of scattering intensities at the illumination position. Consequently, this technique is sensitive to density fluctuations on length scales significantly smaller than the illuminated area. This information is not available from the measurement modes discussed thus far, as is shown in Fig. 4 where a wall of a diatom girdle shows details in dark-field imaging, which are not visible in transmission or phase-contrast images, indicating different nano-structure on the sub-100 nm length scale.

Since the detector is fully pixelated, one can gauge by software the momentum transfer, i.e., the length scale, of interest. However, we note that for such $q$-dependent contrast, a smaller annulus illuminated on the detector is beneficial. The flexibility of the instrument and, in particular, the detector makes such small-angle X-ray scattering (SAXS) mapping measurements easily possible and as efficient as the "standard" STXM imaging modes [21]. As with any STXM, the instrument is fully compatible with complementary techniques such as spatially resolved fluorescence measurements.

## 3. Conclusions

In conclusion, recent developments in area detector technology have made possible to use CCDs or hybrid pixel detectors as efficient and flexible detectors in STXM applications. Detection schemes are highly adaptable and allow, *inter alia*, measuring differential phase contrast. By integrating the DPC signal in two dimensions the phase can be recovered allowing almost arbitrary imaging modes. Furthermore, dark-field imaging and SAXS mapping can be realized with high $q$ resolution.

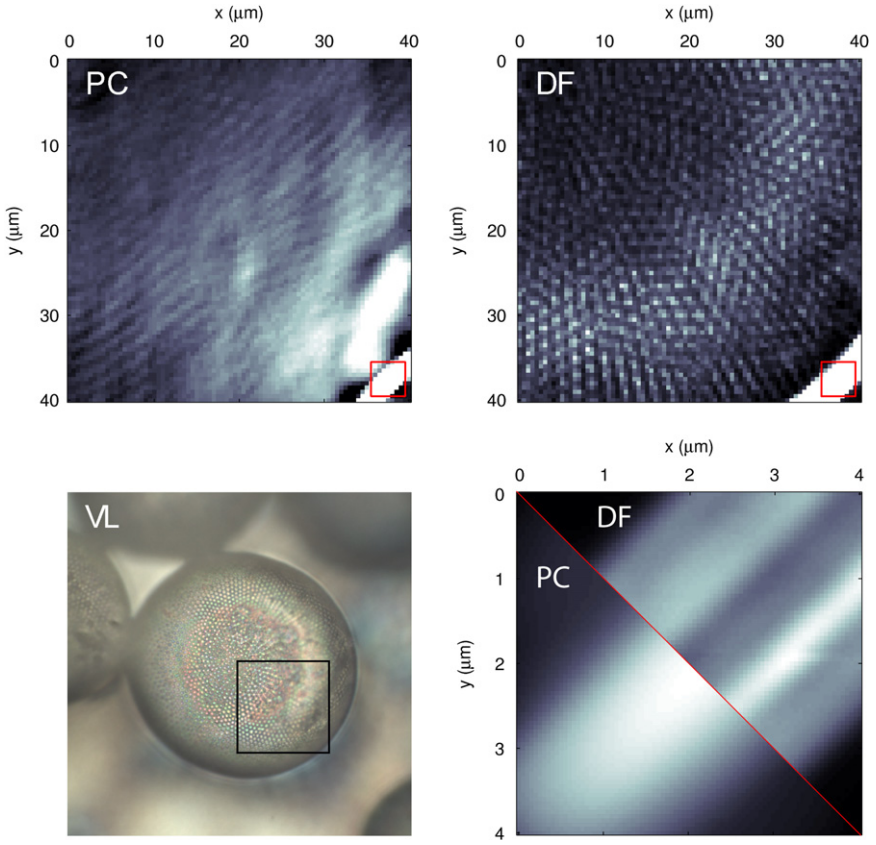


**Fig. 4.** A demonstration of dark-field imaging, as described in the text. Shown is a diatom in valve view, of which a visible light micrograph (VL) with field of view $1.2 \times 1.2\,mm^2$ is shown in the lower left as overview. Upper left, an integrated phase contrast (PC) image; upper right, a dark-field (DF) image. The complementary contrast is evident in the portule pattern, clearly enhanced in the dark field. Fields of view are $40 \times 40\,\mu m$. In the lower right is a direct comparison between phase contrast and dark-field images of the girdle wall. The location of this detail is marked by red square in the upper images. (For interpretation of the references to colour in this figure legend, the reader is referred to the web version of this article.)

We used a fully pixelated detector for the quantitative characterization of the complex-valued optical transmission function at 6.2 keV of a variety of specimens and demonstrated 50 nm resolution. The resolution of all of these imaging techniques is limited by the spatial extent of the illuminating probe. For even higher resolutions, we note that the fully pixelated detectors can be used to Nyquist-sample the diffraction pattern from the coherently illuminated region. Coherent diffractive imaging-related techniques can then be used to increase resolution significantly beyond the probe size [22–24].

## Acknowledgements

We thank O. Marti, U. Nolte and P. Walther, Ulm University, Germany, for the stained-cell sample (Fig. 3), and A. Beran, Istituto Nazionale di Oceanografia e di Geofisica Sperimentale (OGS), Italy, and B. Kaulich, Elettra, for the diatom sample (Fig. 4). Further, we acknowledge technical support at the cSAXS beamline by X. Donath and help during the experiments by I. Johnson and J. Viereck. P.T. acknowledges financial support from the Fonds Québécois de la recherche sur la nature et les technologies (FQRNT).

## References

[1] N. Dekkers, H. Delang, Detection method for producing phase and amplitude images simultaneously in a scanning transmission electron microscope, Philips Tech. Rev. 37 (1) (1977) 1–9.

[2] P. Hawkes, Half-plane apertures in TEM, split detectors in STEM and ptychography, J. Opt. 9 (4) (1978) 235–241.

[3] G.R. Morrison, M. Browne, Dark-field imaging with the scanning-transmission X-ray microscope, Rev. Sci. Instrum. 63 (1) (1992) 611–614.

[4] J. Cowley, Configured detectors for STEM imaging of thin specimens, Ultramicroscopy 49 (1–4) (1993) 4–13.

[5] M. Feser, C. Jacobsen, P. Rehak, G. DeGeronimo, Scanning transmission X-ray microscopy with a segmented detector, January 2003, doi:10.1051/jp4:20030138.

[6] M. Feser, B. Hornberger, C. Jacobsen, G.D. Geronimo, P. Rehak, P. Holl L. Strueder, Integrating Silicon detector with segmentation for scanning transmission X-ray microscopy, Nucl. Instrum. Methods A 565 (2) (2006) 841–854 , doi:10.1016/j.nima.2006.05.086.

[7] G.R. Morrison, B. Niemann, Differential phase contrast X-ray microscopy, in: J. Thiema, G. Schmahl, D. Rudolph, E. Umbach (Eds.), X-Ray Microscopy and Spectromicroscopy, Springer Verlag, Berlin, 1998.

[8] G.R. Morrison, W. Eaton, R. Barrett, P. Charalambous, STXM imaging with a configured detector, January 2003, doi:10.1051/jp4:20030141.

[9] B. Kaulich, D. Bacescu, J. Susini, C. David, E.D. Fabrizio, G.R. Morrison, P. Charalambous, J. Thieme, T. Wilhein, J. Kovav, D. Cocco, M. Salome, O. Dhez, T. Weitkamp, S. Cabrini, D. Cojoc, A. Gianoncelli, U. Vogt, M. Pornar, M. Zangrando, M. Zacchigna, M. Kiskinova, Twinmic—A European twin X-ray microscopy station commissioned at ELETTRA, in: Proceedings of the 8th International Conference X-ray Microscopy, vol. 7, 2006, pp. 22–25.

[10] S. Vogt, H.N. Chapman, C. Jacobsen, R. Medenwaldt, Dark field X-ray microscopy: the effects of condenser/detector aperture, Ultramicroscopy 87 (1–2) (2001) 25–44.

[11] P. Kraft, A. Bergamaschi, C. Broennimann, R. Dinapoli, E.F. Eikenberry, B. Henrich, I. Johnson, A. Mozzanica, C.M. Schlepuetz, P.R. Willmott, B. Schmitt, Performance of single-photon-counting PILATUS detector modules, J. Synchrotron. Radiat. 16 (2009) 368–375 , doi:10.1107/S0909049509009911.

[12] K. Jefimovs, O. Bunk, F. Pfeiffer, D. Grolimund, J.F. van der Veen, C. David, Fabrication of Fresnel zone plates for hard X-rays, January 2007, doi:10.1016/j.mee.2007.01.112.

[13] K. Jefimovs, J. Vila-Comamala, T. Pilvi, J. Raabe, M. Ritala, C. David, Zone-doubling technique to produce ultrahigh-resolution X-ray optics, Phys. Rev. Lett. 99 (26) (2007) 264801 , doi:10.1103/PhysRevLett.99.264801.

[14] M.G. Nomarski, Microinterferometre differentiel a ondes polarisees, J. Phys. Radium 16 (1955) S9–S13.
[15] D. Paganin, T. Gureyev, S. Mayo, A. Stevenson, Y. Nesterets, S. Wilkins, X-ray omni microscopy, J. Microsc. Oxford 214 (2004) 315–327.
[16] M. Arnison, K. Larkin, C. Sheppard, N. Smith, C. Cogswell, Linear phase imaging using differential interference contrast microscopy, J. Microsc. Oxford 214 (2004) 7–12.
[17] C. Kottler, C. David, F. Pfeiffer, O. Bunk, A two-directional approach for grating based differential phase contrast imaging using hard X-rays, Opt. Express 15 (3) (2007) 1175–1181.
[18] M.D. de Jonge, B. Homberger, C. Holzner, D. Legnini, D. Paterson, I. McNulty C. Jacobsen, S. Vogt, Quantitative phase imaging with a scanning transmission X-ray microscope, Phys. Rev. Lett. 100 (16) (2008) 163902 , doi:10.1103/PhysRevLett.100.163902.
[19] W.H. Press, S.A. Teukolsky, W.T. Vetterling, B.P. Flannery, Numerical Recipes in C, second ed., Cambridge University Press, Reading, 1992.
[20] P. Thibault, M. Dierolf, C.M. Kewish, A. Menzel, O. Bunk, F. Pfeiffer, Contrast mechanisms in scanning transmission X-ray microscopy, Phys. Rev. A 80 (4) (2009) 043813.
[21] O. Bunk, M. Bech, T.H. Jensen, R. Feidenhans'l, T. Binderup, A. Menzel, F. Pfeiffer, Multimodal X-ray scatter imaging, New J. Phys. 11 (2009) 123016 , doi:10.1088/1367-2630/11/12/123016.
[22] J.M. Rodenburg, H. Faulkner, A phase retrieval algorithm for shifting illumination, Appl. Phys. Lett. 85 (20) (2004) 4795–4797 , doi:10.1063/1.1823034.
[23] J.M. Rodenburg, A.C. Hurst, A.G. Cullis, B.R. Dobson, F. Pfeiffer, O. Bunk, C. David, K. Jefimovs, I. Johnson, Hard-X-ray lensless imaging of extended objects, Phys. Rev. Lett. 98 (3) (2007) 034801 , doi:10.1103/PhysRevLett.98.034801.
[24] P. Thibault, M. Dierolf, A. Menzel, O. Bunk, C. David, F. Pfeiffer, High-resolution scanning X-ray diffraction microscopy, Science 321 (5887) (2008) 379–382 , doi:10.1126/science.1158573.